Applied Nanoscience (2023) 13:5239–5249
https://doi.org/10.1007/s13204-022-02746-6

ORIGINAL ARTICLE

Magnetic properties and nanocrystallization process in Co–(Me)–Si–B amorphous ribbons

Yulia Nykyruy[1] · Stepan Mudry[1] · Yuriy Kulyk[1] · Anatoliy Borisyuk[2]

Received: 11 June 2022 / Accepted: 9 December 2022 / Published online: 28 December 2022

Abstract

Magnetic properties of amorphous $Co_{70}Fe_3Mn_{3.5}Mo_{1.5}Si_{11}B_{11}$ and $Co_{73}Fe_1Mn_3Mo_1Si_{13}B_9$ alloys, manufactured in the form of ribbons by rapid cooling from the melt, were studied using vibrating sample magnetometer and thermo-magnetic methods. The Curie point (648 K and 683 K), coercive force (180 A/m and 40 A/m), and saturation magnetization (83 Am^2/kg and 85 Am^2/kg) were defined. The nanocrystallization process of the amorphous $Co_{70}Fe_3Mo_{1.5}Mn_{3.5}Si_{11}B_{11}$ and $Co_{73}Fe_1Mo_1Mn_3Si_{13}B_9$ alloys were studied by DTA, X-ray diffraction, and using the thermo-magnetic method in the high magnetic field 800 kA/m. The crystallization onset temperatures of the alloys were defined as about 787 K and 729 K, respectively. The effect of a magnetic field on the crystallization behavior, revealed in a notable crystallization onset temperature decrease, was observed. The structure evolution induced by the isothermal annealing at temperature 753 K was studied and the X-ray diffraction structure analyses revealed nanocrystallization with hcp-Co, fcc-Co, and Co_3B phases. FESEM studies revealed a nanoscale and flower-like structure on the ribbon surface after annealing at 753 K.

Keywords Co-based amorphous alloy · Nanocrystallization · DTA · Magnetic properties · Flower-like structure

Introduction

Amorphous metal alloys are non-crystalline solids that are characterized by a structure with short-range order. This structural characteristic of AMC provides isotropic physical and mechanical properties of these materials (Inoue and Hashimoto 2001). Due to the absence of a crystalline structure, amorphous metal alloys (AMS) have high strength and elasticity, excellent corrosion and wear resistance, excellent soft magnetic properties, which ensures their effective use in Electrical and Electronic Technology Engineering, Microelectromechanical Systems MEMS, Medicine, Military Equipment, and others (Herzer 2013, Nabiałek 2020).

Among these materials, AMA based on the Co–Si–B system deserve special attention, and for several last decades, have found applications in sensor elements, cores, choke coils, etc. (Životský et al. 2016; Nosenko et al. 2020). Due to their magnetic properties, they are used in the production of magnetic screens/shielding, read heads, information recording, storage devices, and high-frequency power applications (Hasegawa 2004; Ackland et al. 2018). Depending on the type of hysteresis loop, these materials find applications in current and power transformers, common mode chokes (CMC's), magnetic amplifiers (MagAmps), magnetic field and current sensors, pulse compression applications, etc. (Liebermann 1993). AMC based on the Co–Si–B system, in addition to extremely low re-magnetization losses and high saturation magnetization, also have unique frequency characteristics and practically zero magnetostriction (Russew and Stojanova 2016; Karolus et al. 2005; Torrens-Serra et al. 2008). Due to this circumstance, its soft magnetic properties are insensitive to mechanical impacts. Thanks to a wide application, the studies of cobalt-based amorphous/nanocrystalline alloys and their physical properties are of great importance nowadays.

AMA are metastable and transform to a crystalline state at high temperatures or long-term aging. Therefore, the processes of crystallization of AMA were studied by many researchers to clarify the main parameters that determine the time–temperature stability of AMC. It is known that dopants and variations of the content of metalloid group elements

✉ Yulia Nykyruy
yuliya.nykyruy@lnu.edu.ua

[1] Metal Physics Department, Ivan Franko National University of Lviv, Lviv, Ukraine

[2] Department of Applied Physics and Nanomaterial Science, Lviv Polytechnic National University, Lviv, Ukraine

can lead to the optimization of operating parameters. Hence, from a technological as well as fundamental viewpoint, it is important to investigate the effects of the annealing process on the amorphous structure of the Co–(Me)–Si–B alloys. In this paper, we provide our studies on the thermal stability and magnetic properties of Co–B–Si AMA doped with Fe, Mn, and Mo, as well as nanocrystallization features under thermal annealing.

Materials and methods

The amorphous cobalt-based alloys with compositions $Co_{70}Fe_3Mn_{3.5}Mo_{1.5}Si_{11}B_{11}$ and $Co_{73}Fe_1Mn_3Mo_1Si_{13}B_9$ were manufactured in the form of the ribbons by rapid cooling from the melt using the melt-spinning technique. The ribbon thickness and width were about 25 μm and 1 cm, respectively. The as-obtained ribbons were investigated by the DTA method using synchronous thermal analyzer Linseis STA PT 1600 under dynamic argon atmosphere (~6 L per hour). Heating was performed at the rate of 10 K/min from 293 K up to 973 K. Magnetic measurements were performed using a vibrating sample magnetometer. Re-magnetization curves of the studied samples were recorded in a magnetic field from –300 kA/m to + 300 kA/m. Since the use of saturating magnetic fields is a prerequisite for performing quantitative magnetic phase analysis, the specific saturation magnetization (σ_s) and its temperature dependence were measured in the magnetic field of 800 kA/m.

To study the nanocrystallization process, the isothermal annealing technique at temperature 753 ± 5 K with different exposures in the range of 5–240 min was used. The annealed ribbon structure was investigated using the back-scattered X-ray diffraction (XRD) method. X-ray diffraction patterns of the samples were obtained on an automated X-ray diffractometer DRON-3 in Cu Kα radiation ($\lambda = 1.5418$ Å), monochromatized by reflection from the plane (002) of the pyrographite single crystal mounted on the diffracted beam. The patterns were analyzed by Lorentzian function fitting of the XRD main maximum (Nykyruy et al. 2018). The full width at half maximum (FWHM) of the fitted Lorentzian function was used to evaluate the average cluster size by the formulas: $L_{cl} = 2\pi/\Delta s, s = (4\pi\sin\theta)/\lambda$, where Δs—full width at half maximum (FWHM), 2θ—scattering angle. Phases, which crystallize under annealing, were determined by the interpretation of diffraction peaks' positions. The average grain size of crystallites (L_{cr}) was determined using formula (Langford and Wilson 1978; Sokolov et al. 1992): $L_{cr} = \lambda/\beta\cos(\theta)$, where $\beta = B - b$; B and b—full width at half maximum (FWHM) for the investigated and reference samples respectively, 2θ—scattering angle.

The ribbon surface structure was also studied by field emission scanning electron microscopy (FESEM), using the Hitachi S-4100 microscope with a secondary electron detector. The average size of grains was measured using the freeware software ImageJ.

Results and discussion

The DTA curves for the as-quenched amorphous ribbons were obtained in the temperature range of 293 K up to 973 K (Fig. 1), and details of obtained exothermic DTA peaks are summarized in Table 1. For the $Co_{70}Fe_3Mo_{1.5}Mn_{3.5}Si_{11}B_{11}$ alloy, one exothermic DTA peak with a maximum at 791.6 K was clearly detected (Fig. 1a). The exothermic peak on the DTA curve for amorphous material is usually related to a crystallization process, and the peak onset point at 786.6 K was interpreted as crystallization onset temperature (T_{xs}^{DTA}).

The DTA curve of the $Co_{73}Fe_1Mo_1Mn_3Si_{13}B_9$ alloy (Fig. 1b) demonstrates one clear exothermic peak with a maximum at 837.8 K, besides much smaller peak can be highlighted at the temperature of 736.7 K. So, the onset point of this peak (724.4 K) was interpreted as the crystallization onset temperature (T_{xs}^{DTA}). The temperature range between the two peaks is about 101 K. The presence of two peaks reveals the two-stage crystallization process, corresponding to the multi-stage model of crystallization. So, minor changes in the chemical composition (up to 3%) have significantly affected the crystallization behavior of studied alloys.

The slight substitution of cobalt elements on iron or manganese affected both the onset temperature of crystallization and the crystallization model (Panda et al. 2005, Bayri et al. 2016). As was shown by Bayri et al. (2016), the partial substitution of Fe, Mn, or Mo for Co elements in Co–Si–B amorphous alloy has led to increasing the activation energy, indicating that a small amount of substitution elements produces a decreased rate of the crystallization kinetics. The changes in activation energy were attributed to the relative size of the substitution elements. In studies (Gencer et al. 2013; Zhai et al. 2014), it has been concluded that crystallization kinetic is closely related to the relative size of substitution atoms. The substitution elements of Fe (1.56 Å), Mn (1.61 Å), and Mo (1.90 Å) have a larger atomic size than Co (1.52 Å). The larger atoms enhance the potential barrier and hinder the diffusion of atoms in the crystallization process of amorphous alloys.

The temperature dependencies of specific saturation magnetization $\sigma_s(T)$ for $Co_{70}Fe_3Mo_{1.5}Mn_{3.5}Si_{11}B_{11}$ and $Co_{73}Fe_1Mo_1Mn_3Si_{13}B_9$ amorphous alloys were measured in the magnetic field of 800 kA/m (~10 kOe) in the temperature range of 290–950 K. It should be noted that at temperatures 650–800 K, the decomposition of homogeneous amorphous phase and the formation of regions with different chemical compositions, different short-range or

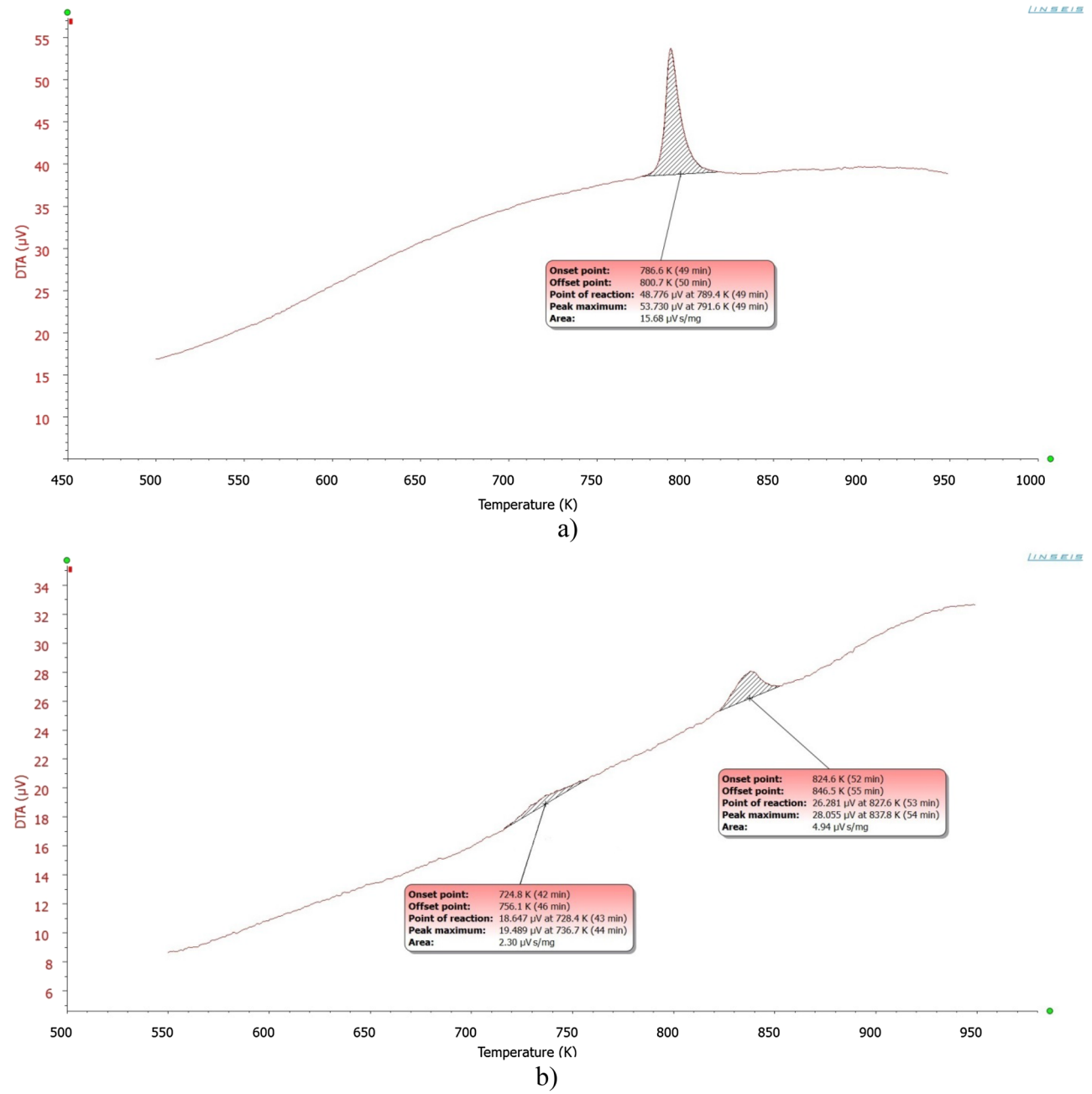

Fig. 1 DTA curves of the as-quenched alloys: **a** $Co_{70}Fe_3Mo_{1.5}Mn_{3.5}Si_{11}B_{11}$, **b** $Co_{73}Fe_1$ $Mo_1Mn_3Si_{13}B$

Table 1 Results of DTA measurements

Alloy	Peak	Onset point, K	Offset point, K	Point of reaction, K	Peak maximum, K	Area μVs/mg
$Co_{70}Fe_3Mo_{1.5}Mn_{3.5}Si_{11}B_{11}$	1	786.6	800.7	789.4	791.6	15.68
$Co_{73}Fe_1Mo_1Mn_3Si_{13}B_9$	1	724.4	756.1	728.4	736.7	2.30
	2	824.6	846.5	827.6	837.8	4.94

long-range order occurs, which means the transformation from a homogeneous to a heterogeneous structure. Magnetic phase analysis of heterogeneous systems is carried out in saturated magnetic fields since only the saturation magnetization does not depend on structural factors (shape, size, stress state of the phase) and is a unique function of the phase composition, linearly dependent on the number of phases. As a result of the generalization of estimates of the required intensity of the saturating magnetic field in a number of works, values from 6 to 10 kOe are recommended for the magnetic phase analysis of the alloys. (Coey 2010; Betancourt-Cantera et al. 2019; Clifford et al. 2014; Meziane et al. 2016). Obtained thermo-magnetic (TM) curves are presented in Fig. 2a. The saturation magnetization of both alloys as expected decreases with temperature increasing up to the Curie temperature (T_C) that marks the ferromagnetic–paramagnetic transition, at which $\sigma_s \rightarrow 0$. The TM curves have revealed quite different values of T_C for investigated ribbons that are about 648 and 683 K, respectively (see Table 2). For $Co_{70}Fe_3Mo_{1.5}Mn_{3.5}Si_{11}B_{11}$ alloy, the σ_s is close to zero in the range of 720–750 K and reached a minimum value of 1.4 A*m^2/kg at temperature 740.8 K, but for the $Co_{73}Fe_1Mo_1Mn_3Si_{13}B_9$ alloy, the σ_s is not so close to zero and reached a minimum value of 3.7 A*m^2/kg at a temperature around 700.4 K. Further temperature increase resulted in a drastic rise of σ_s up to 20–25 Am^{2}kg^{-1} at the temperatures 748.9 K and 703.8 K, respectively. This magnetization behavior indicated the magnetic transition from a paramagnetic to a ferromagnetic state, due to the crystallization of the amorphous phase and the formation of crystalline phases with much higher Curie temperature. The temperature interval of paramagnetic phase existence for amorphous $Co_{70}Fe_3Mo_{1.5}Mn_{3.5}Si_{11}B_{11}$ was wide, about ~ 100 K, while for $Co_{73}Fe_1Mo_1Mn_3Si_{13}B_9$ was very narrow, about ~ 20 K.

The thermo-magnetic method is often used to study the crystallization process in amorphous ferromagnets due to the sensitivity of magnetization to the formation of crystalline grains (Fernández et al. 2000; Vasić et al. 2022).Using the experimental TM curve, the following parameters of the crystallization process can be determined: the temperature of crystallization onset at which the rise of σ_s begins (T_{xs}); the crystallization temperature, that corresponds to the maximal rate of σ_s rise (T_x); the temperature range of crystal phase formation ($\Delta T_x = T_x — T_{xs}$) that corresponds to σ_s rise (Zakharenko et al. 2000). These parameters observed for investigated alloys are summarized in Table 2. It is worth noting that the $\sigma_s(T)$ curve related to $Co_{73}Fe_1Mo_1Mn_3Si_{13}B_9$ alloy was characterized by two intervals of σ_s increasing that could be interpreted as the crystallization of two ferromagnetic phases, and the crystallization of the alloy proceeds through a two-stage model. The crystallization temperature of the second stage is about 839.8 K. And the only one interval of σ_s increasing was observed on the TM curve related to $Co_{70}Fe_3Mo_{1.5}Mn_{3.5}Si_{11}B_{11}$ that corresponds to the one-stage crystallization process.

The results of thermo-magnetic measurements correlate with the DTA results in particular in observing one-stage and two-stage crystallization processes; however, the values of crystallization onset temperature obtained by the DTA method (T_{xs}^{DTA}) were higher than the values obtained by the TM curves (T_{xs}™). This can be partially explained by different heating rates at DTA and TM studies (Babych et al. 2008; Zhang et al. 2021), but differences between T_{xs}^{DTA} and T_{xs}™ values for both alloys were quite significant to be satisfied with this explanation, and the effect of the magnetic field on the crystallization behavior should be considered. A number of papers reported the influence of a high magnetic field (H) on the crystallization of Fe-based amorphous alloys, showing that a high magnetic field accelerated the formation of the α-Fe phase (Wolfus et al. 1987, Odonera et al. 2013, Odonera et al. 2014, Zhuang et al. 2016). The magnetic field accelerates the crystallization process by increasing the free-energy separation between the amorphous and crystalline phases by the value $\Delta M*H$, where ΔM is the difference in the magnetic moment between the phases. The increase of the magnetic energy decreases the activation energy required for the nucleation of the crystal phase. It is also considered that the enhancement of the crystallization rate is caused by the increase of the nucleation rate due to decreasing of the activation energy by the magnetic field. Since the Co-based and Fe-based amorphous materials are of one type, the similar effect of magnetic field on the crystallization of Co-based alloys should be taken into account. The difference between T_x^{DTA} and T_x™ values for $Co_{70}Fe_3Mn_{3.5}Mo_{1.5}Si_{11}B_{11}$ alloy was about 38 K and for $Co_{73}Fe_1Mn_3Mo_1Si_{13}B_9$ about 25 K that revealed enhanced sensitivity to a high magnetic field of the first one alloy. But for a more detailed study of the high magnetic field effect on the crystallization process of Co-based AMAs, additional studies are required.

Re-magnetization curves of the studied samples were recorded in a magnetic field from –300 kA/m to + 300 kA/m. The hysteresis curves of the magnetic moment are presented in Fig. 2b, and saturation magnetization σ_s and coercivity H_C of the studied alloys are summarized in Table 2. Determination of the coercivity values was carried out using the simulation of the area of demagnetization of the hysteresis loop. The higher value of σ_s and lower value of H_C was observed for the $Co_{73}Fe_1Mn_3Mo_1Si_{13}B_9$ alloy (85 A*m^2/kg and 40 A/m, respectively). A slightly lower value of σ_s, but a significantly greater value of H_C was obtained for the $Co_{70}Fe_3Mo_{1.5}Mn_{3.5}Si_{11}B_{11}$ alloy (83 A*m^2/kg and 180 A/m, respectively). Analysis of the magnetization curves showed that in the region of weak magnetic fields, the magnetization increased in proportion to the external strength magnetic field, and in a strong magnetic field (above 17–20 kA/m), there was saturation.

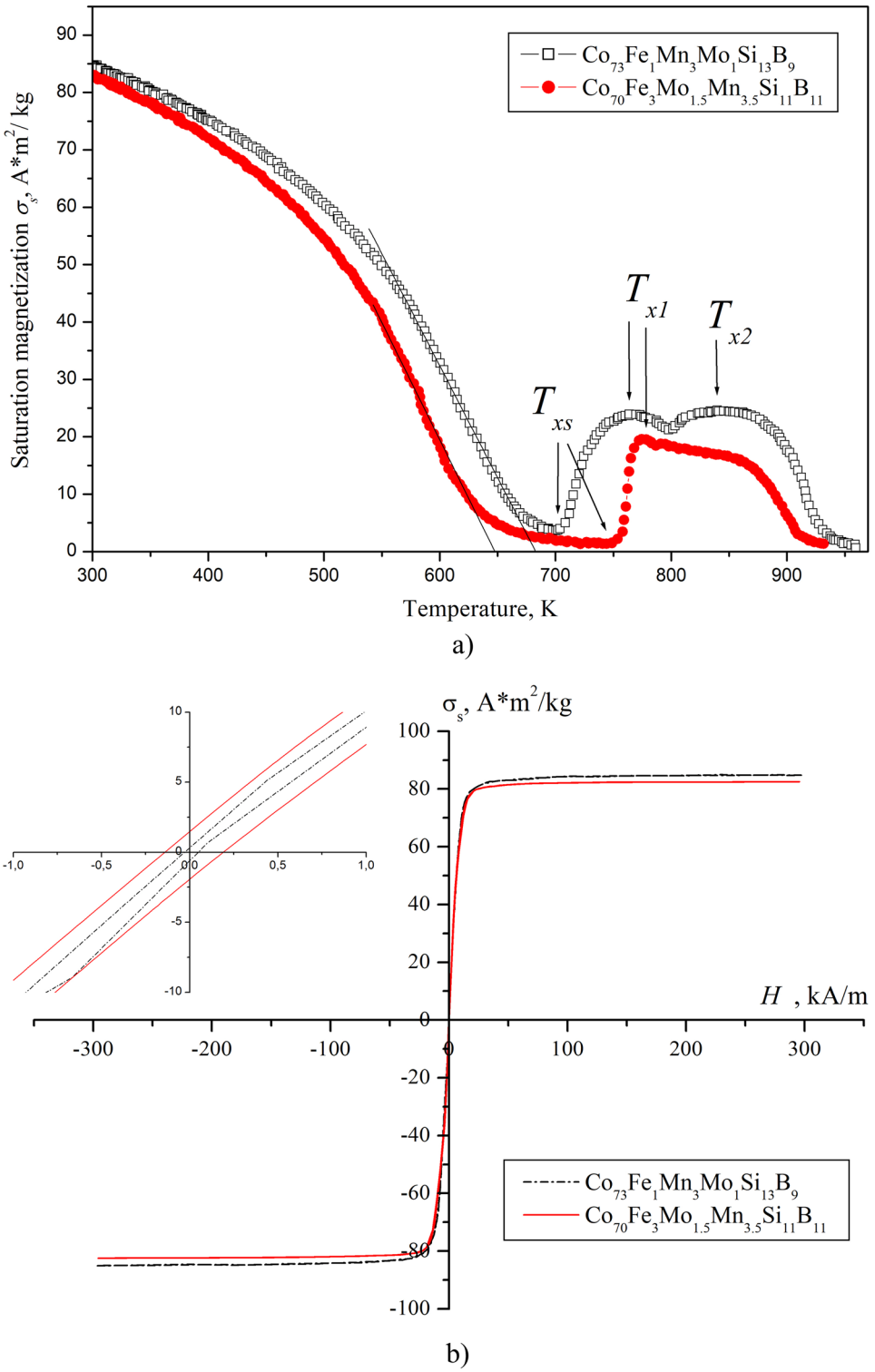

Fig. 2 The thermo-magnetic **a** and hysteresis **b** curves for $Co_{70}Fe_3Mo_{1.5}Mn_{3.5}Si_{11}B_{11}$ and $Co_{73}Fe_1Mo_1Mn_3Si_{13}B_9$ amorphous alloys

Table 2 Results of magnetic measurements

No	Alloy composition	T_C, K	σ_s, Am^2 /kg	H_c, A/m	T_{xs}™, K	T_x™, K		ΔT_x™, K
						I stage	II stage	
1	$Co_{70}Fe_3Mn_{3.5}Mo_{1.5}Si_{11}B_{11}$	647.7	83	180	748.8	774.4	–	25.6
2	$Co_{73}Fe_1Mn_3Mo_1Si_{13}B_9$	682.8	85	40	703.8	763.8	839.8	60.0

The magnetization of the amorphous ribbon occurs by slightly shifting the boundaries of the domains and the reverse rotation of the vector of spontaneous magnetization. The values of the coercivity were about 40 A/m and 180 A/m, which corresponded to the average coercivity for soft magnetic materials (Konieczny et al. 2010; Nykyruy et al. 2022). Saturation requires quite strong magnetic fields, while the residual magnetization is small.

The values of Curie point and the saturation magnetization are determined by the origin of the ferromagnetic phase (crystal lattice, electronic structure of atoms, chemical composition of the phase). While, the coercivity is a structurally dependent value and depends on elastic stresses, shape, and dimensions of the ferromagnetic phase. So, the difference in Curie points of studied alloys can be caused by partial substitution of Fe, Mn, or Mo for Co elements and the difference in the coercivity values can be conditioned by structural differences of the as-quenched alloys, which in turn also depend on composition.

It can be interesting to compare the parameters of these Co-based alloys with amorphous Fe-based alloys because these two groups of alloys are the most common in manufacturing. Earlier, we studied the magnetic properties of $Fe_{73.5}Nb_3Cu_1Si_{15.5}B_7$ alloy using the same vibrating sample magnetometer (Mudry et.al 2014). Comparing the parameters of the Co-based with the Fe-based amorphous alloys, it can be mentioned the higher values of Curie temperature (for about 50–80 K), lower values of crystallization onset temperature (for about 50–100 K), and lower values of saturation magnetization (for about 50 Am^2/kg) for the Co-based alloys.

The structures of the as-quenched ribbons were studied by the X-ray diffraction method (Cu-Kα) and the shape of the XRD curves characterized an amorphous structure (Fig. 3); no intensity peaks from a crystalline phase were detected. The curves were fitted by the two-peak Lorentzian functions, and the FWHP of the first peaks was used to obtain the average size of regions of coherent scattering (clusters). According to this, the average size of the clusters was about 17.2 Å for $Co_{73}Fe_1Mo_1Mn_3Si_{13}B_9$ and 16.1 Å for $Co_{70}Fe_3Mo_{1.5}Mn_{3.5}Si_{11}B_{11}$ alloy. The difference in the average size of the nanoclusters of the two alloys was too small to cause about a fourfold difference in coercivity, so it can be assumed that the difference in coercivity was due to change in the content of elements.

It is known that the amorphous state is metastable and structure evolution to an equilibrium state occurs under the influence of external factors passing through the nanocrystallization process. The nanocrystallization behavior of amorphous Co–(Me)–Si–B alloys usually depends on alloying components. As was studied previously, upon primary crystallization of $Co_{66.5}Fe_{4.0}Mo_{1.5}Si_{16.0}B_{12.0}$, the formation of fcc-Co and metastable Co_3B nanocrystalline phases was observed, and further heating of the alloy leads to the disappearance of the Co_3B phase and to the formation of Co_2B and Co_2Si phases (Girzhon et al. 1998). The nanocrystalline fcc-Co, hcp-Co, Co_3B, and Co_2Si were observed in $Co_{74}Fe_1Mn_3Si_{13}B_9$ after 1-h annealing at ~ 770 K (Abrosimova et al. 2021). Besides, the secondary crystal products in similar alloys are the so-called 23–6 phases, which are of the Fm3m space group, and follow the $Cr_{23}C_6$ prototype with $(Fe, Co)_{23}B_6$ (DeGeorge et al. 2015). The $Co_{23}B_6$ phase

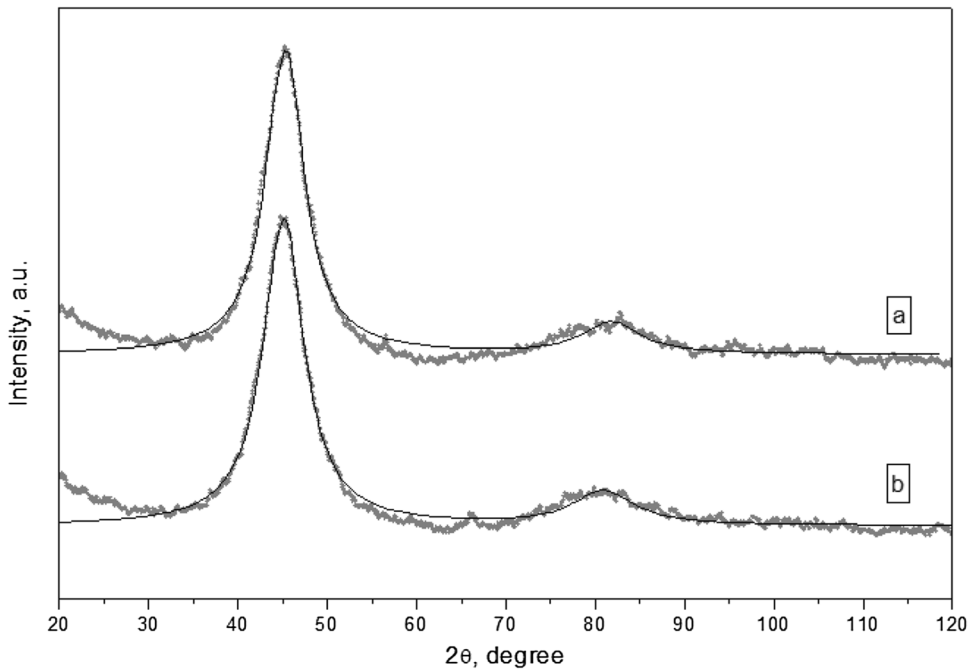

Fig. 3 X-Ray diffraction intensity curves of the as-quenched alloys: **a** $Co_{73}Fe_1Mo_1Mn_3Si_{13}B_9$, **b** $Co_{70}Fe_3Mo_{1.5}Mn_{3.5}Si_{11}B_{11}$

was also observed in $Co_{70}Fe_5Si_{10}B_{15}$ and similar type alloy (Vasić et al. 2018, Bednarčík et al. 2004). Secondary crystallization is the subject of much investigation in magnetic amorphous and nanocomposites because the Co–B phases are detrimental to the magnetic properties of the nanocomposites, and it limits the long-term and thermal stability of their operation in device applications (DeGeorge et al. 2015). Understanding crystallization kinetics of this phase and factors that induce the process, in particular exposure at high temperatures, allows to predict the thermal stability and determine operating conditions.

Structure evolution in $Co_{70}Fe_3Mo_{1.5}Mn_{3.5}Si_{11}B_{11}$ and $Co_{73}Fe_1Mo_1Mn_3Si_{13}B_9$ amorphous alloys was studied under isothermal annealing at temperature 753 ± 5 K with a duration of up to 240 min. The annealing temperature of about 753 K was close to the crystallization onset temperature of $Co_{70}Fe_3Mn_{3.5}Mo_{1.5}Si_{11}B_{11}$ alloy. X-Ray diffraction patterns of the ribbons after annealing are shown in Fig. 4. It is clear that the transition from cluster structure to nanocrystalline is accompanied by cluster size increasing. The characteristic feature of this transition is an appearance of symmetry in the atomic distribution in nanocrystals. Such symmetry can be revealed by a detailed analysis of diffraction patterns. In the case of cluster structure, we observe only one diffraction peak, whereas in the case of nanocrystals, more peaks should be pronounced. To study the phase composition of the annealed ribbons, we used the analysis by the multi-peaks Lorentzian function fitting of the XRD main maximum, and the results are summarized in Table 3. The main maximums of the XRD curves obtained from the as-quenched ribbons can be correctly approximated by the one-peak Lorentzian function (Fig. 3), representing an amorphous structure. After the 30 min annealing of $Co_{70}Fe_3Mn_{3.5}Mo_{1.5}Si_{11}B_{11}$ alloy, the XRD curve was accompanied by weak reflexes that reveal some quantity of nanocrystalline phase of cobalt with a hexagonal close-packed lattice (hcp-Co). After 120 min annealing, the $Co_{70}Fe_3Mn_{3.5}Mo_{1.5}Si_{11}B_{11}$ ribbon became completely nanocrystalline. The phase composition of $Co_{70}Fe_3Mn_{3.5}Mo_{1.5}Si_{11}B_{11}$ sample, annealed during 240 min, consisted of hcp-Co, ($a = 2.5184 \pm 0.0005$ Å, $c = 4.0065 \pm 0.0011$ Å), with an average grain size $L_{cr} \approx 15.0 \pm 2.0$ nm; fcc-Co ($a = 3.5311 \pm 0.0008$ Å), $L_{cr} \approx 55.0 \pm 6.0$ nm; Co_2Si ($a = 4.9251 \pm 0.0009$ Å, $b = 3.7781 \pm 0.0006$ Å, $c = 7.1688$ Å), $L_{cr} \approx 50.0 \pm 5.5$ nm; and Co_3B ($a = 5.2084 \pm 0.0010$ Å, $b = 6.6242 \pm 0.0010$ Å,

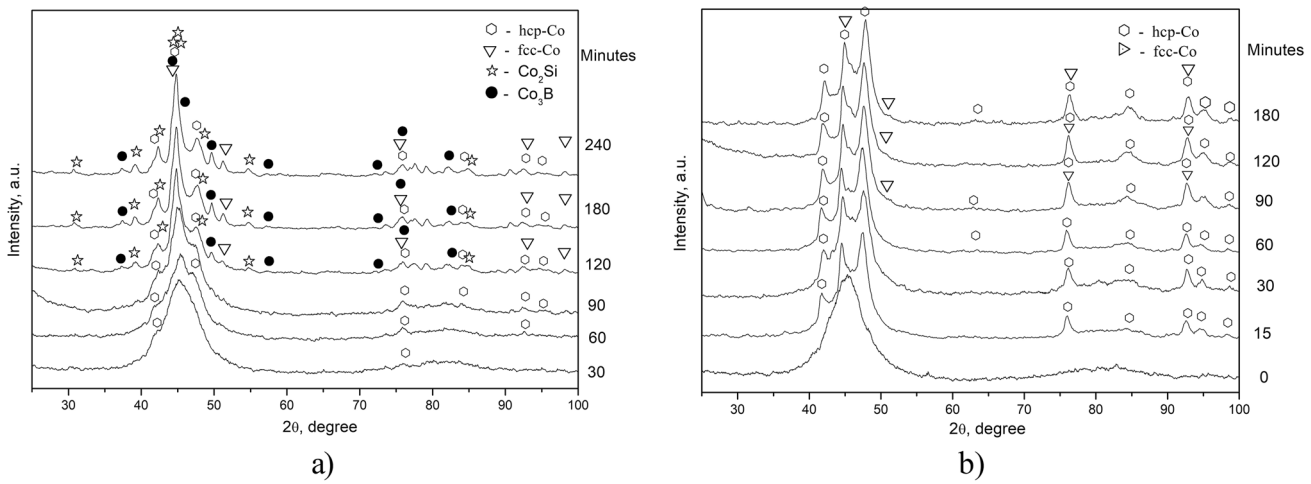

Fig. 4 X-Ray diffraction intensity curves of the ribbons after annealing at 753 K **b** upon different exposures **a** $Co_{70}Fe_3Mo_{1.5}Mn_{3.5}Si_{11}B_{11}$, **b** $Co_{73}Fe_1Mo_1Mn_3Si_{13}B_9$

Table 3 The composition of alloys after annealing at the specified exposure times

$Co_{70}Fe_3Mo_{1.5}Mn_{3.5}Si_{11}B_{11}$		$Co_{73}Fe_1Mo_1Mn_3Si_{13}B_9$,	
Exposure time, min	Composition	Exposure time, min	Composition
30	A + hcp-Co	15	A + hcp-Co
60	A + hcp-Co	30	A + hcp-Co
90	A + hcp-Co	60	A + hcp-Co
120	hcp-Co + fcc-Co + Co_3B + Co_2Si	90	A + hcp-Co + fcc-Co
180	hcp-Co + fcc-Co + Co_3B + Co_2Si	120	A + hcp-Co + fcc-Co
240	hcp-Co + fcc-Co + Co_3B + Co_2Si	180	A + hcp-Co + fcc-Co

$c = 4.4204 \pm 0.0010$ Å), $L_{cr} \approx 35.0 \pm 4.0$ nm. The XRD results correlate with DTA results confirming one-stage crystallization model for the $Co_{70}Fe_3Mn_{3.5}Mo_{1.5}Si_{11}B_{11}$ alloy.

Another crystallization process was observed for the $Co_{73}Fe_1Mo_1Mn_3Si_{13}B_9$ alloy. For this alloy, the annealing temperature was higher than the value of T_{xs}^{DTA} but lower than the temperature of the second DTA peak. The XRD curve from the sample annealed for 15 min was also accompanied by weak reflexes revealing some quantity of the nanocrystalline hcp-Co phase. The increasing annealing time has resulted in the strengthening of reflexes from hcp-Co phase and appearing of weak reflexes from fcc-Co phase. No Co–B or Co–Si phases were revealed. This is consistent with the two-stage model of the nanocrystallization process: the Co crystallization occurs in the first stage, while the Co–B or Co–Si crystallization occurs in the second stage. The phase composition of $Co_{73}Fe_1Mo_1Mn_3Si_{13}B_9$ sample, annealed during 180 min, consisted mainly of hcp-Co, ($a = 2.5053 \pm 0.0005$ Å, $c = 4.0621 \pm 0.0012$ Å), with an average grain size of $L \approx 15.0 \pm 2.0$ nm.

It is worth noting that, in cobalt, the martensite hcp–fcc transition takes place at a temperature range of about ~ 660–740 K (Bauer et al. 2011). This is lower than the annealing temperature of 753 K. After cooling, a significant fraction of the high-temperature fcc phase is typically retained in the microstructure (i.e., the reverse fcc–hcp transformation is incomplete). The residual fcc phase stands as another microstructure parameter affecting the mechanical performance of the material, in addition to typical parameters such as grain size, dislocation density, crystallographic texture, etc. (Knapek et al. 2020).

Results of FESEM studies revealed the smooth amorphous-like structure of the as-quenched alloy and the fine-grained structure of the ribbons after annealing. Figures 5a, b present the surface structure of free upon amorphization ribbon side and ribbon edge, respectively, for the as-quenched alloy. The low contrast of the image generated by secondary electrons indicates favor of a smooth and uniform surface, which is inherent in the amorphous structure. Figures 5c, d present the surface structure after annealing for 60 min and 180 min, accordingly. Given the results of the XRD study for these two samples, we can conclude partial and complete crystallization with a fine nanograin structure. The size of grains obtained from Fig. 5c varied in the range of 20–100 nm and the average value was defined as about 50 nm. The nanograins are visible on a smooth background and it can be interpreted as partial crystallization of the amorphous phase, which is consistent with the XRD result for this sample. The size of grains obtained from Fig. 5d varies in the range of 20–200 nm and the average grain size was defined as about 65 nm which is close to the value obtained by XRD for this sample. No smooth background is visible in the figure, only a nanograined structure is seen that is consistent with the XRD result for this sample.

The image in Fig. 5e, d resembled a flower-like structure similar to that obtained for Co_3O_4 by Cai et al. 2019, Kannagi et al. 2020, Kumar, et al. 2020. In general, flower-like structures were discovered for several materials: flower-like 3D Ag–Au hetero-nanostructures (Zhang, et al. 2018), hierarchical flower-like Ag nanostructures (Zhang et al. 2017), and flower-like Fe_3O_4/MnO_2 microspheres (Ma et al. 2019). Flower-like structure formation was described as a self-assembled process (Parveen and Cho 2016, Sheng et al. 2011). A self-assembly strategy for the fabrication of well-defined 3D flower-like hierarchical structures of Ni/Co-layered double hydroxides by chemical co-precipitation under the mild reaction condition (55 °C) was described in Li et al. (2016). As for cobalt, Du and co-workers developed flower-like structures of Co/CoO, using a two-step hydrothermal process followed by a subsequent annealing process (Lv, Hualiang et al. 2015). They described the role of the temperature for flower-like structure formation, with a suitable annealing treatment of the composite at 400 °C which is essential. When heated at a lower temperature, 300 °C, or a higher annealing temperature, 500 °C, they did not get flower-like microstructures. In view of this, we can assume that the thermal annealing of the Co–(Me)–Si–B alloy in the temperature range of 673–773 K (400–500 °C) is suitable for the formation of flower-like structures on the surface of the Co–(Me)–Si–B ribbon.

The flower-like structure contained numerous very thin flakes, with layer spacing appropriate for electromagnetic scattering in a frequency bandwidth ranging from 13.8–18 GHz. Furthermore, the porous flower-like microstructure acted as an excellent lightweight microwave absorption material (Bhosale et al. 2020). A super-hydrophobicity of coatings was attributed to micro–nano flower-like structure (Khorsand, 2015). All this arouses increased interest in continuing our research on the nanostructuring of amorphous Co–(Me)–Si–B alloys.

Conclusion

Magnetic properties and thermally induced nanocrystallization behavior in $Co_{70}Fe_3Mo_{1.5}Mn_{3.5}Si_{11}B_{11}$ and $Co_{73}Fe_1Mo_1Mn_3Si_{13}B_9$ amorphous alloys were studied by means of techniques: DTA, vibrating sample magnetometer, thermo-magnetic, and X-ray. According to the DTA, the crystallization onset temperatures of these alloys are 787 K and 724 K, respectively. However, the effect of a magnetic field should be taken into account when considering the thermal stability or crystallization process since significantly lower values of crystallization onset temperatures (749 K and 704 K, respectively) were observed by the

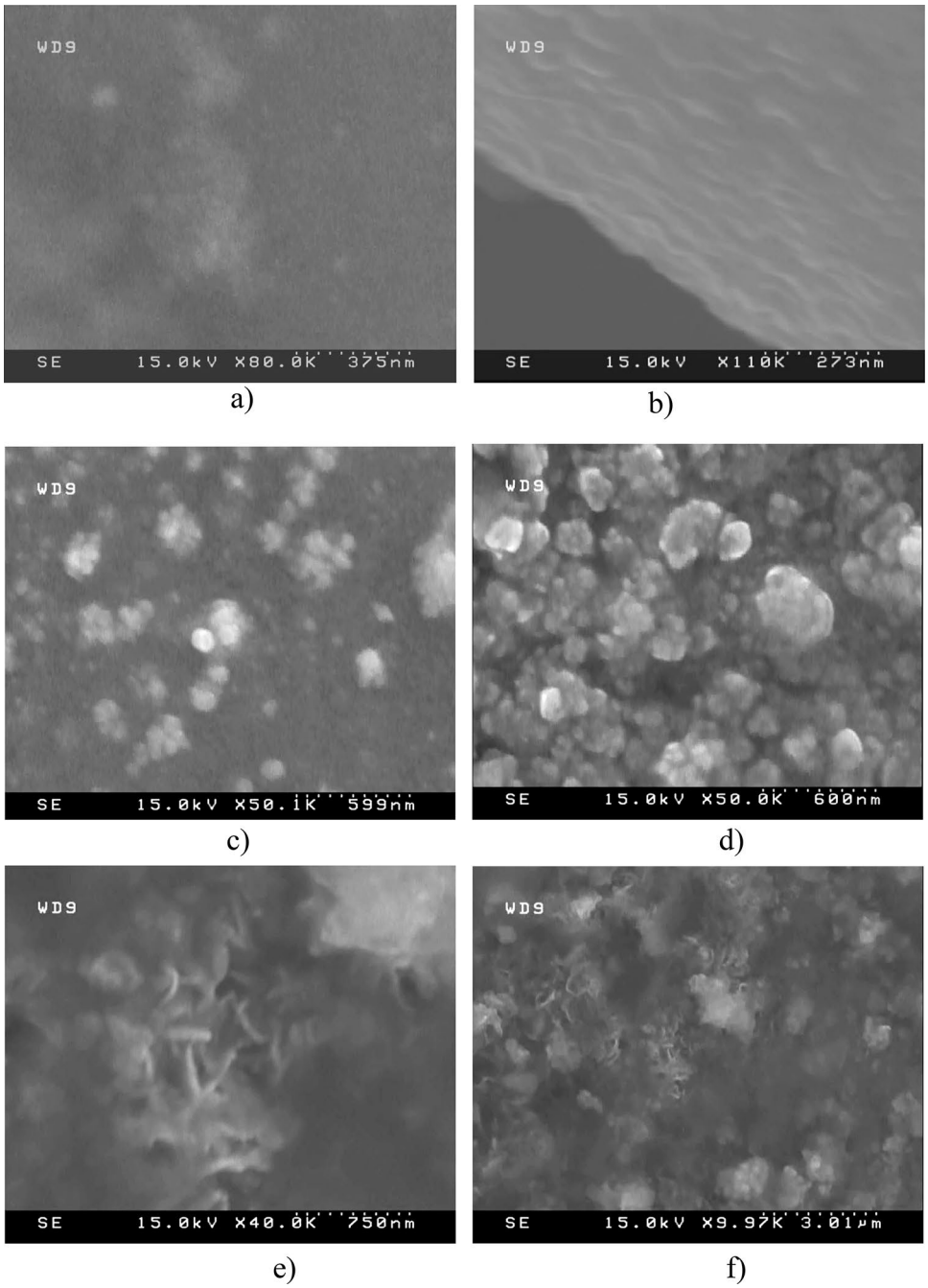

Fig. 5 FESEM images of $Co_{70}Fe_3Mo_{1.5}Mn_{3.5}Si_{11}B_{11}$ surface: **a** free upon amorphization side of the as-quenched ribbon, **b** as-quenched ribbon edge, **c** fine grains after annealing at exposure 60 min, **d** fine grains structure after annealing at exposure 180 min, **e** and **d** flower-like structure

thermo-magnetic method when applying a high magnetic field (about 800 kA/m).

Amorphous alloys with very similar chemical compositions showed quite different thermal stability and magnetic properties. It was observed that the nanocrystallization process of the $Co_{73}Fe_1Mo_1Mn_3Si_{13}B_9$ alloy corresponds to a two-stage crystallization model, while $Co_{70}Fe_3Mo_{1.5}Mn_{3.5}Si_{11}B_{11}$ corresponds to a single-stage crystallization model. The thermal stability of the $Co_{70}Fe_3Mo_{1.5}Mn_{3.5}Si_{11}B_{11}$ alloy was higher than that of the $Co_{73}Fe_1Mo_1Mn_3Si_{13}B_9$ alloy by almost 60 K. Both alloys in the as-quenched (as prepared) state were characterized by the amorphous structure, and the saturation magnetization values of both alloys were quite close, 85 Am^2 /kg and 83 Am^2 /kg, but the values of coercivity and Curie points were significantly different: for $Co_{73}Fe_1Mo_1Mn_3Si_{13}B_9$ alloy, the coercivity was 40 A/m and Curie point was 683 K, while for the $Co_{70}Fe_3Mo_{1.5}Mn_{3.5}Si_{11}B_{11}$ alloy, the coercive force was 180 A/m and the Curie point was 648 K. A slight variation in the percentage of elements significantly changed the process of nanocrystallization in amorphous Co–Fe–Mn–Mo–Si–B alloys. From a technological point

of view, the $Co_{73}Fe_1Mo_1Mn_3Si_{13}B_9$ alloy is more promising because it has less coercive force. In addition, the two-stage crystallization process, in which the unwanted boride phase was formed in the second stage, allows to carry out the optimization annealing to form a nanocrystalline fine structure without Co–B that can potentially improve the magnetic properties. A flower-like structure was detected on the ribbon surface after annealing at 753 K, a structure that is potentially able to improve the surface properties of the material.

Acknowledgements We are grateful to our colleagues at the G.V. Kurdyumov Institute for Metal Physics of the N.A.S. of Ukraine for their assistance in obtaining samples under investigation and to Andriy Horyn, PhD, Senior Researcher, and Chief of Inter-faculty Laboratory of Differential Thermal Analysis of Ivan Franko National University of Lviv for the assistance in the DTA study. The authors would like to acknowledge the University of Wurzburg for providing the equipment for the FESEM investigation.

Data availability The data will be available based on the request.

Declarations

Conflict of interest The authors declare no conflict of interest.

References

Abrosimova G, Volkov N, Chirkova V, Aronin A (2021) The effect of the type of component crystal lattice on nanocrystal formation in Co-based amorphous alloys. Mater Lett 297:129996. https://doi.org/10.1016/j.matlet.2021.129996

Ackland K, Masood A, Kulkarni S, Stamenov P (2018) Ultra-soft magnetic Co-Fe-B-Si-Nb amorphous alloys for high frequency power applications. AIP Adv 8(5):056129. https://doi.org/10.1063/1.5007707

Babych MG, Zakharen'ko MI, Semen'ko MP, Kunytsky Yu A, Leonov DS (2008) Peculiarities of Cobalt Based Amorphous Alloys Crystallization. Nanosys Nanomater Nanotechnol 6(1):237–250

Bauer R, Jägle EA, Baumann W, Mittemeijer EJ (2011) Kinetics of the allotropic hcp–fcc phase transformation in cobalt. Philos Mag 91:437–457. https://doi.org/10.1080/14786435.2010.525541

Bayri N et al (2016) Crystallisation kinetics of $Co_{75-x}M_xSi_{15}B_{10}$ (M = Fe, Mn, Cr and x = 0, 5) amorphous alloys. Acta Phys Pol, A. https://doi.org/10.12693/APhysPolA.129.84

Bednarčík J, Kováč J, Kollár P, Roth S, Sovák P, Balcerski J, Polanski K, Švec T (2004) Crystallization of CoFeSiB metallic glass induced by long-time ball milling. J Non-Cryst Solids 337(1):42–47. https://doi.org/10.1016/j.jnoncrysol.2004.03.105

Betancourt-Cantera JA, Sánchez-De JF, Bolarín-Miró AM, Torres-Villaseñor G, Betancourt-Cantera LG (2019) Magnetic properties and crystal structure of elemental cobalt powder modified by high-energy ball milling. J Mater Res Technol. https://doi.org/10.1016/j.jmrt.2019.07.048

Bhosale SV, AlKobaisi M, Jadhav RW, Jones LA (2020) Flowerâ like superstructures: structural features, applications and future perspectives. Chem Rec. https://doi.org/10.1002/tcr.202000129

Cai Y, Xu J, Guo Y, Liu J (2019) Ultrathin, polycrystalline, two-dimensional Co3O4 for low-temperature CO oxidation. ACS Catal. https://doi.org/10.1021/acscatal.8b04064

Clifford DM, El-Gendy AA, Lu AJ, Pestov D, Carpenter EE (2014) Room temperature synthesis of highly magnetic cobalt nanoparticles by continuous flow in a microfluidic reactor. J Flow Chem JFC 4(3):148–152

Coey J (2010) Magnetism and Magnetic Materials. Cambridge University Press, Cambridge. https://doi.org/10.1017/CBO9780511845000

DeGeorge V, Zoghlin E, Keylin V, McHenry M (2015) Time temperature transformation diagram for secondary crystal products of Co-based Co-Fe-B-Si-Nb-Mn soft magnetic nanocomposite. J Appl Phys 117(17):17A329. https://doi.org/10.1063/1.4916759

Egami T (1978) Structural relaxation in amorphous alloys - compositional short range ordering. Mater Res Bullet 13(6):557–562. https://doi.org/10.1016/0025-5408(78)90178-2

Fernández A, Pérez MJ, Tejedor M, Madurga V (2000) Thermo-magnetic analysis of amorphous (CoxFe1−x)735Nb3Cu1Si135B9 metallic glasses. J Magn Magn Mater 221(3):338–344. https://doi.org/10.1016/s0304-8853(00)00493-5

Gencer H, Izgi T, Kolat VS, Bayri N, Atalay S (2013) The crystallisation kinetics, magnetic and magnetocaloric properties of $Gd_{55}Co_{20}Fe_5Al_{20-x}Si_x$ (x = 0, 5, 10, 15) alloys. J Non-Cryst Solids 379:185. https://doi.org/10.1016/j.jnoncrysol.2013.08.009

Girzhon VV, Rudnev YuV, Anpilogov DI, Smolyakov AV (1998) Crystallization of metal-metalloid glasses under laser heating. Scripta Mater. https://doi.org/10.1016/S1359-6462(98)00244-9

Hasegawa R (2004) Applications of amorphous magnetic alloys. Mater Sci Engi 375–377:90–97. https://doi.org/10.1016/j.msea.2003.10.258

Herzer G (2013) Modern soft magnets: amorphous and nanocrystalline materials. Acta Mater 61(3):718–734. https://doi.org/10.1016/j.actamat.2012.10.040

Inoue A, Hashimoto K (eds)(2001) Amorphous and nanocrystalline materials. Adv Mater Res. https://doi.org/10.1007/978-3-662-04426-1

Kannagi K, Purushothaman KK, Suganya P, Sethuraman B (2020) Synthesis and characterization of 3Dflower like Co_3O_4 for supercapacitor application. Proc Adv Mater Eng Technol. https://doi.org/10.1063/5.0019465

Karolus M., Kwapuliński P., Chrobak D., Haneczok G., Chrobak A., J. Mater. Process. Tech. 162–163, 203 (2005

Khorsand S, Raeissi K, Ashrafizadeh F, Arenas MA (2015) Superhydrophobic nickel–cobalt alloy coating with micro-nano flower-like structure. Chemi Eng J. https://doi.org/10.1016/j.cej.2015.03.076

Knapek M, Minárik P, Dobroň P, Šmilauerová J, Celis MM, Hug E, Chmelík F (2020) The effect of different thermal treatment on the allotropic fcc↔hcp transformation and compression behavior of polycrystalline cobalt. Materials 13(24):5775. https://doi.org/10.3390/ma13245775

Konieczny J, Borisjuk A, Pashechko M, Dobrzanski L (2010) Magnetic properties of Co-based amorphous ribbon under cyclic heating and cooling. Journal of Achievements in Materials and Manufacturing Engineering. 42:(1–2).

Kumar M, Bhatt V, Yun J-H (2020) Hierarchical 3D micro flower-like Co3O4 structures for NO2 detection at room temperature. Physics Lett A. https://doi.org/10.1016/j.physleta.2020.126477

Langford JI, Wilson AJC (1978) Scherrer after sixty years: a survey and some new results in the determination of crystallite size. J Appl Cryst 11:102–113

Li T, Li G, Li L, Liu L, Xu Y, Ding H, Zhang T (2016) Large-scale self-assembly of 3D flower-like hierarchical Ni/Co-LDHs microspheres for high-performance flexible asymmetric supercapacitors. ACS Appl Mater Inter. https://doi.org/10.1021/acsami.5b10158

Liebermann H (1993) Rapidly Solidified Alloys. Processes-Structures-Properties-Applications. by CRC Press.

Lv H, Liang X, Ji G, Zhang H, Du Y (2015) Porous three-dimensional flower-like co/coo and its excellent electromagnetic absorption properties. ACS Appl Mater Interfaces 7(18):9776–9783. https://doi.org/10.1021/acsami.5b01654

Ma M, Yang Y, Chen Y, Wu F, Li W, Lyu P, Ma Y, Tan W, Huang W (2019) Synthesis of hollow flower-like Fe3O4/MnO2/Mn3O4 magnetically separable microspheres with valence heterostructure for dye degradation. Catalysts 9(7):589. https://doi.org/10.3390/catal9070589

Meziane L, Salzemann C, Aubert C, Gérard H, Petit C, Petit M (2016) Hcp cobalt nanocrystals with high magnetic anisotropy prepared by easy one-pot synthesis. Nanoscale 8(44):18640–18645. https://doi.org/10.1039/c6nr05792f

Mudry SI, Nykyruy YS (2014) Laser induced structure transformation in $Co_{70}Fe_3Mn_{3.5}Mo_{1.5}B_{11}Si_{11}$ amorphous alloy. Mater Sci-Pol 32:28–33. https://doi.org/10.2478/s13536-013-0152-2

Mudry SI, Nikirui YS, Borisyuk AK (2014) Effect of laser processing on the structure and magnetic characteristics of an amorphous $Fe^{73}._5Nb_3Cu_1Si1_5.5B_7$ alloy. Inorg Mater 50:358–364. https://doi.org/10.1134/S0020168514040116

Nabiałek, Marcin (2020) Fabrication Methods for Bulk Amorphous Alloys in Inamuddin. Rajender Boddula, Mohd Imran Ahamed, Abdullah M. Asiri (eds.) Alloy Materials and Their Allied Applications, 1–26, © 2020 Scrivener, Publishing LLC. https://doi.org/10.1002/9781119654919.ch1

Nosenko AV, Kyrylchuk VV, Semen'ko MP, Nowicki M, Marusenkov A, Mika TM, Nosenko VK (2020) Soft magnetic cobalt based amorphous alloys with low saturation induction. J Magnetism Magnetic Mater. https://doi.org/10.1016/j.jmmm.2020.167328

Nykyruy YS, Mudry SI, Kulyk YO, Zhovneruk SV (2018) Structural transformation in Fe73.5Nb3Cu1Si15.5B7 amorphous alloy induced by laser heating. Lasers Manufact Mater Process 5(1):31–41. https://doi.org/10.1007/s40516-017-0051-1

Nykyruy YS, Mudry SI, Kulyk YO, Lapinski M (2020) Nanocrystallization and phase formation in Fe73.5Nb3Cu1Si15.5B7 amorphous ribbon under laser heating. Mater Sci-Poland 38(4):526–534. https://doi.org/10.2478/msp-2020-0064

Nykyruy Yu, Mudry S, Shtablavyi I, Borisyuk A, Ya T, Gnilitskyi I (2022) Formation of laser-induced periodic surface structures on amorphous Fe- and Co-based alloys and its impact on magnetic properties. Mater Chem Phys. https://doi.org/10.1016/j.matchemphys.2022.126317

Odonera R, Kimura S, Watanabe K, Lee S, Yokoyama Y, Makino A, Koyama K (2013) Magnetic field effects on crystallization of iron-based amorphous alloys. Mater Trans, 2013, 54(2), 188-191.https://doi.org/10.2320/matertrans.M2012242

Odonera R, Kimura S, Watanabe K, Yokoyama Y, Makino A, Koyama K (2014) Influences on the crystallization kinetics of iron-based amorphous alloys under high magnetic fields. J Alloys Compd. https://doi.org/10.1016/j.jallcom.2014.03.080

Panda AK, Kumari S, Chattoraj I, Svec P, Mitra A (2005) Effect of Fe addition on the crystallization behaviour and Curie temperature of CoCrSiB-based amorphous alloys. Philos Mag 85(17):1835–1845. https://doi.org/10.1080/14786430500098934

Parveen N, Cho MH (2016) Self-assembled 3D flower-like nickel hydroxide nanostructures and their supercapacitor applications. Sci Rep. https://doi.org/10.1038/srep27318

Reisho O, Shojiro K, Kazuo W, Sangmin L, Yoshihiko Y, Akihiro M, Keiichi K (2013) Magnetic field effects on crystallization of iron-based amorphous alloys. Mater Trans 54(2):188–191. https://doi.org/10.2320/matertrans.M2012242

Russew K, Stojanova L (2016) Properties and applications of amorphous metallic alloys. Glassy Metals. https://doi.org/10.1007/978-3-662-47882-0_13

Sheng X, Wang L, Chen G, Yang D (2011) Structures and their use as templates to prepare CuS particles. J Nanomater. https://doi.org/10.1155/2011/280216

Sokolov AP, Kisliuk A, Soltwisch M, Quitmann D (1992) Medium range order in glasses: comparison of raman and diffraction measurements. Phys Rev Lett 69:1540–1543. https://doi.org/10.1103/PhysRevLett.69.1540

Torrens-Serra J, Roth S, Rodriguez-Viejo J, Clavaguera-Mora MT (2008) Effect of Nb in the nanocrystallization and magnetic properties of FeNbBCu amorphous alloys. J Non-Cryst Solids 354:5110

Vasić MM, Žák T, Pizúrová N, Roupcová P, Minić DM, Minić DM (2018) Thermally induced microstructural transformations and anti-corrosion properties of $Co_{70}Fe_5Si_{10}B_{15}$ amorphous alloy. J Non-Cryst Solids. https://doi.org/10.1016/j.jnoncrysol.2018.08.017

Vasić MM, Žák T, Minić DM (2022) Kinetics and influence of thermally induced crystallization of Fe, Ni-containing phases on thermo-magnetic properties of $F_{e4}0N_{i4}0_{B1}2S_i8$ amorphous alloy. J Therm Anal Calorim 147:3543–3551. https://doi.org/10.1007/s10973-021-10819-x

Wolfus Y, Yeshurun Y, Felner I, Wolny J (1987) Crystallization kinetics in amorphous ferromagnets effect of temperature and magnetic field. Philosophical Magazine B 56(6):963–968. https://doi.org/10.1080/13642818708215332

Zakharenko M, Brud'ko O, Babich M, Nosenko V, Tsvetkova T, Stelmakh O (2000) Thermo-magnetic study of the $Fe_{80}Si_6B_{14}$-based soft magnetic glasses. J Magn Magn Mater 215–216:313–315. https://doi.org/10.1016/s0304-8853(00)00303-6

Zhai FQ, Pineda E, Duarte MJ, Cresp D (2014) Role of Nb in glass formation of Fe–Cr–Mo–C–B–Nb BMGs. J Alloys Comp 604:157. https://doi.org/10.1016/j.jallcom.2014.03.095

Zhang C, Hao R, Zhao B, Fu Y, Hao Y, Liu Y (2017) Novel synthesis of hierarchical flower-like silver assemblies with assistance of natural organic acids for surface-enhanced Raman spectroscopy. J Mater Sci, 52(19):11391–11401. https://doi.org/10.1007/s10853-017-1292-2

Zhang Y, Yang C, Xue B, Peng Z, Cao Z, Mu Q, Xuan L (2018) Highly effective and chemically stable surface enhanced Raman scattering substrates with flower-like 3D Ag-Au hetero-nanostructures. Sci Rep 8(1):898. https://doi.org/10.1038/s41598-018-19165-9

Zhang BH, Liu JH, Zhou HT (2021) Comprehensive study of the crystallization behavior, thermal stability, and magnetic properties of Co665Si155B12Fe4Ni2 amorphous ribbon. J Non-Cryst Solids. https://doi.org/10.1016/j.jnoncrysol.2021.121132

Zhang, Congyun at al. Novel synthesis of hierarchical flower-like silver assemblies with assistance of natural organic acids for surface-enhanced Raman spectroscopy, J Mater Sci, doi:https://doi.org/10.1007/s10853-017-1292-2

Zhuang YX, Wang WB, Han BT, Xing PF (2016) Effect of high magnetic field on crystallization behavior of Fe 83 B 10 C 6 Cu 1 amorphous alloy. J Alloys Compd 684:649–655. https://doi.org/10.1016/j.jallcom.2016.05.158

Životský O, Titov A, Jirásková Y, Buršík J, Hendrych A, Hrabovská K, Tsepelev VS (2016) Surface and bulk magnetic anisotropy in bilayered CoSiB/FeNbCuSiB and FeNbSiB/FeSiB ribbons. J Alloys Compd 681:402–411. https://doi.org/10.1016/j.jallcom.2016.04.243